Transition from dendritic to planar growth and banded structure formation in rapidly solidified alloys

Massimo Conti

Dipartimento di Matematica e Fisica, Università di Camerino and Istituto Nazionale di Fisica della Materia, 62032 Camerino, Italy

To study the formation of the so-called *banded structures*, we simulated the rapid directional solidification of a binary alloy in two dimensions using the phase-field model. We found that an oscillatory instability of the solidification front, driven by the loss of interfacial equilibrium, forces the interface velocity v and temperature T_I to describe an orbit in the (T_I,v) plane. In the low-velocity portion of the cycle the planar front breaks into a dendritic pattern, resulting in a strong solute microsegregation. As a consequence, the solidified region shows a highly irregular solute distribution. At high velocities the dendritic pattern is suppressed and the solid phase grows with uniform composition. Due to the fast transients of the process our results, which reflect the full time-dependent interface dynamics, show only a qualitative agreement with the phenomenological model of Carrard *et al.* [Acta Metall. Mater. **40**, 983 (1992)], which is based on a quasistationary approximation. [S1063-651X(98)00111-1]

PACS number(s): 81.10.Aj, 05.70.Ln, 64.70.Dv

I. INTRODUCTION

In rapidly solidified alloys, at growth rates close to the absolute stability limit, a different and unexpected microstructure has been observed, consisting of alternating dark and light bands parallel to the solidification front. In this so-called *banded structure* [1–4] the dark bands are formed of periodic cells or dendrites, growing antiparallel to the heat flux direction. At eutectic composition, the typical lamellar structure has also been observed. The light bands show a uniform composition, equal to the nominal concentration of the alloy. The total band spacing ranges from 0.3 to 1.5 μm. The physical origin of the banded structures represented an intriguing problem that remained unsolved for several years, as they were not expected within the classic Mullins-Sekerka analysis [5]. Decisive progress was achieved when the linear stability analysis was revisited by Coriell and Sekerka [6]: To account for nonequilibrium effects such as solute trapping at the moving interface, they introduced a velocity-dependent segregation coefficient $k(v)$, defined as the ratio c_s/c_l of the solute concentration in the growing solid to that in the liquid at the interface. Subsequently, Merchant and Davis [7] incorporated into the problem the results of the continuous growth model of Aziz [8] and Aziz and Kaplan [9], allowing the segregation coefficient k and the interface temperature T_I to depend on the interface velocity v in a thermodynamically consistent way. These studies led to the identification of an oscillatory instability characterized by an infinite wavelength along the solid-liquid front; it was argued that this instability should be responsible for the band formation [10]. The approach to the problem was refined by Huntley and Davis [11] and Karma and Sarkissian [12], who relaxed the hypothesis of infinite thermal diffusivity and accounted for the effects of the latent heat diffusion. The most relevant results they achieved evidenced a reduction of the parameters range where the oscillatory instability should occur; moreover, the release of the latent heat at the interface drives a restabilization mechanism at zero wave number. Nu-

merical simulations, conducted in one dimension with both the Green's functions technique [13] and the phase-field model [14], showed that the oscillatory instability actually leads, in a nonlinear regime, to time-periodic changes in the interface velocity and interface temperature, which reflect in periodic variations of the solute concentration along the growth direction.

While the periodicity of the banded structure is clearly related to the oscillatory instability of the solidification front, to explain the emergence of a dendritic pattern, responsible for the microsegregation characteristics of the dark bands, a wider perspective was required and the problem had to be addressed at least in two dimensions. Carrard *et al.* [10] proposed a phenomenological model describing the formation of the banded structure as a periodic breakdown between dendritic and planar front growth. As they observed, in a range of interfacial temperatures rapid solidification can proceed in stable and steady conditions at two distinct velocities, corresponding to the dendritic branch of the diffusional model (lower value) and to the planar growth branch (higher value). At intermediate velocity values the driving force for solidification (the dynamic undercooling) is a decreasing function of the associated flux (the growth rate), resulting in unstable planar solutions. When the isotherm velocity is fixed in this region steady growth is prevented and the solidification front undergoes periodic transitions between the planar and dendritic branches. Starting from the above considerations, the authors estimated the width of the dark and light bands and their predictions were in agreement with the experimental data. However, detailed information on the time-dependent dynamics of the solidification pattern, which results in the formation of the banded structure, is still lacking.

In the present study the rapid solidification of a binary alloy, driven by a moving temperature field, is simulated in two dimensions through the phase-field model. Due to numerical tractability, the effect of the latent heat diffusion is neglected; nevertheless, we hope to capture the most relevant characteristics of the process. In a region of the parameters space the oscillatory instability of the solidification front

forces the interface velocity and temperature to follow a cycle in the (T_I, v) plane. In the low-velocity portion of the cycle the planar front breaks into a dendritic pattern, resulting in strong and irregular solute microsegregation. At high velocity the process enters the absolute stability region and the dendritic pattern is suppressed: As a consequence, the solid phase grows with uniform composition. The results of our simulations show a qualitative agreement with the picture of the process given by Carrard *et al.* [10]; however, we detected also significant deviations whose origin will be analyzed and discussed.

The scheme of this paper is as follows. In Sec. II the governing equations of the model will be presented. In Sec. III details of the numerical method will be given. In Sec. IV the results of the numerical simulations will be presented and discussed. The conclusions will follow in Sec. V.

II. PHASE-FIELD MODEL

The directional solidification of an ideal solution of components A (solvent) and B (solute) is described in terms of the scalar phase field ϕ, the local solute concentration c, and temperature T. The field ϕ is an order parameter assuming the values $\phi = 0$ in the solid and $\phi = 1$ in the liquid; intermediate values correspond to the interface between the two phases. The model is developed starting from an entropy formulation [15] and follows the lines suggested by Wheeler, Boettinger, and McFadden [16,17], Caginalp and Xie [18], and Caginalp and Jones [19]. A similar version was the basis of previous numerical studies conducted in both one and two dimensions [20–23]. Full details of the derivation are presented elsewhere [24] and for the sake of conciseness we shall give below only a short review. As a starting point an entropy functional is defined as

$$\mathcal{S} = \int \left[s(e, \phi, c) - \frac{\epsilon^2}{2} |\nabla \phi|^2 \right] dv, \quad (1)$$

where integration is performed over the system volume. The last term in the integrand is a gradient correction to the thermodynamic entropy density s, which depends on the internal energy density e and on the concentration and phase fields through the thermodynamic relations

$$\frac{\partial s}{\partial e} = \frac{1}{T}, \quad \frac{\partial s}{\partial c} = \frac{\mu^A - \mu^B}{T},$$

$$\frac{\partial s}{\partial \phi} = -\frac{1}{T} \frac{\partial}{\partial \phi} [(1-c)\mu^A + c\mu^B], \quad (2)$$

where μ^A and μ^B are the chemical potentials of the solvent and the solute, respectively. A conservation law governs the solute transport

$$\dot{c} = -\nabla \cdot \mathbf{J}_c. \quad (3)$$

To ensure that the local entropy production is always positive, the solute flux can be written in a simple form as

$$\mathbf{J}_c = M_c \nabla \frac{\delta \mathcal{S}}{\delta c}, \quad (4)$$

while the nonconserved dynamics of the phase field ϕ is expressed through

$$\dot{\phi} = M_\phi \frac{\delta \mathcal{S}}{\delta \phi}, \quad (5)$$

where M_c and M_ϕ are positive constants.

Assuming a double-well Ginzburg-Landau free energy for the pure constituents and evaluating the functional derivatives gives

$$\frac{\partial \phi}{\partial t} = M_\phi [\epsilon^2 \nabla^2 \phi - (1-c)\tilde{H}^A(\phi, T) - c\tilde{H}^B(\phi, T)], \quad (6)$$

$$\frac{\partial c}{\partial t} = -\nabla \cdot \left\{ D_c c(1-c) \frac{v_m}{R} [\tilde{H}^A(\phi, T) - \tilde{H}^B(\phi, T)] \nabla \phi \right.$$

$$\left. - D_c \nabla c + D_c c(1-c) \frac{v_m}{R} \tilde{\Gamma}(\phi, T) \nabla T \right\}. \quad (7)$$

In Eqs. (6) and (7) R is the gas constant and v_m is the molar volume. D_c is the solute diffusivity defined as $D_c = (M_c R)/[v_m c(1-c)]$. The function $\tilde{H}^A(\phi, T)$ is defined as

$$\tilde{H}^A(\phi, T) = \frac{dG^A(\phi)}{d\phi} - \frac{dp(\phi)}{d\phi} L^A \frac{T - T^A}{TT^A}, \quad (8)$$

where

$$G^A(\phi) = \tfrac{1}{4} \tilde{W}^A \phi^2 (1-\phi)^2 = \tilde{W}^A g(\phi) \quad (9)$$

is a symmetric double-well potential with equal minima at $\phi = 0$ and 1, scaled by the positive well height $\tilde{W}^A$. L^A and T^A are the latent heat per unit volume and the melting temperature of the pure component A; choosing the function $p(\phi)$ as $p(\phi) = \phi^3 (10 - 15\phi + 6\phi^2)$, the condition is enforced that the bulk solid and liquid are described by $\phi = 0$ and 1, respectively, for every value of temperature [25].

Equations (8) and (9) still hold for $\tilde{H}^B(\phi, T)$ and $G^B(\phi)$ if all the material parameters labeled with the superscript A are replaced with the ones related to the B species. The function $\tilde{\Gamma}(\phi, T)$ is defined as

$$\tilde{\Gamma}(\phi, T) = -\frac{p(\phi)}{T^2} (L^A - L^B). \quad (10)$$

To allow for different diffusivities in the solid and liquid phases in the following D_c will be taken as $D_c = D_s + p(\phi)(D_l - D_s)$, D_l and D_s being the diffusivities in the liquid and in the solid, respectively.

As we neglect the latent heat diffusion, the temperature field is decoupled from the phase and concentration fields and is represented as a traveling wave moving towards the positive x direction with uniform gradient $\tilde{G}$ and constant velocity $\tilde{V}_0$:

$$\frac{\partial T}{\partial t} = -\tilde{V}_0 \frac{\partial T}{\partial x} = -\tilde{V}_0 \tilde{G}. \quad (11)$$

Equations (6), (7), and (11) will be rephrased scaling lengths to some reference length ξ and time to ξ^2/D_l. Allowing M_ϕ to depend on the local composition as $M_\phi = (1-c)M_\phi^A + cM_\phi^B$ and following the lines suggested by Warren and Boettinger [20] to associate the model parameters with the material properties, the governing equations become

$$\frac{\partial \phi}{\partial t} = [(1-c)m^A + cm^B]$$

$$\times [\nabla^2 \phi + (1-c)Q^A(T,\phi) + cQ^B(T,\phi)], \quad (12)$$

$$\frac{\partial c}{\partial t} = \boldsymbol{\nabla} \cdot \{\lambda(\phi)\boldsymbol{\nabla}c - c(1-c)\lambda(\phi)[H^A(\phi,T) - H^B(\phi,T)]$$

$$\times \boldsymbol{\nabla}\phi - c(1-c)\lambda(\phi)\Gamma(\phi,T)\boldsymbol{\nabla}T\}, \quad (13)$$

$$\frac{\partial T}{\partial t} = -V_0 \frac{\partial T}{\partial x} = -V_0 G, \quad (14)$$

where

$$H^{A,B}(\phi,T) = W^{A,B}\frac{dg(\phi)}{d\phi} - L^{A,B}\frac{v_m}{R}\frac{dp(\phi)}{d\phi}\frac{T-T^{A,B}}{TT^{A,B}}$$

$$= \frac{v_m}{R}\tilde{H}^{A,B}(\phi,T), \quad (15)$$

$$Q^{A,B}(\phi,T) = -\frac{\xi^2}{(h^{A,B})^2}\frac{dg(\phi)}{d\phi}$$

$$+ \frac{1}{6\sqrt{2}}\frac{\xi^2 L^{A,B}}{\sigma^{A,B}h^{A,B}}\frac{T-T^{A,B}}{\bar{T}_I}\frac{dp(\phi)}{d\phi}, \quad (16)$$

$$\Gamma(\phi,T) = \frac{v_m}{R}\tilde{\Gamma}(\phi,T), \quad (17)$$

$$\lambda(\phi) = \frac{D_s}{D_l} + p(\phi)\left(1 - \frac{D_s}{D_l}\right), \quad (18)$$

$$V_0 = \tilde{V}_0 \frac{\xi}{D_l}, \quad G = \tilde{G}\xi. \quad (19)$$

In Eq. (16) $\sigma^{A,B}, h^{A,B}$ indicate the surface tension and the interface thickness of the pure components A and B, respectively. $\bar{T}_I$ is the initial (equilibrium) interface temperature. The model parameters $m^{A,B}, W^{A,B}$ depend on the physical properties of the alloy components through

$$m^{A,B} = \frac{\beta^{A,B}\sigma^{A,B}T^{A,B}}{D_l L^{A,B}}, \quad W^{A,B} = \frac{12}{\sqrt{2}}\frac{v_m}{R}\frac{\sigma^{A,B}}{T^{A,B}h^{A,B}}, \quad (20)$$

where $\beta^{A,B}$ is the kinetic undercooling coefficient of pure A or B, which relates the interface undercooling to the interface velocity v through $v = \beta^{A,B}(T^{A,B} - T_I)$.

Anisotropy of surface energy can be accounted for by allowing the parameter ϵ to depend on the angle θ, defined as the angle between the normal to the interface and a fixed direction, the x axis in our calculations. We assume a depen-

TABLE I. Material parameters for the Si-Ge alloy.

Parameter	Silicon	Germanium
Melting temperature (K)	1693	1218
Latent heat (J/cm^3)	4208	2698
Molar volume (cm^3/mole)[a]	12.02	13.64
D_l (cm^2/s)	10^{-5}	10^{-5}

[a]An average value of 12.96 has been taken.

dence $\epsilon(\theta) = \bar{\epsilon}(1 + \gamma \cos 4\theta) = \bar{\epsilon}\eta(\theta)$, enforcing a fourfold symmetry; γ specifies the intensity of the anisotropy. Equation (12) is modified as

$$\frac{\partial \phi}{\partial t} = [(1-c)m^A + cm^B]$$

$$\times \left\{ \boldsymbol{\nabla} \cdot [\eta^2(\theta)\boldsymbol{\nabla}\phi] + \frac{\partial}{\partial y}\left(\eta(\theta)\eta'(\theta)\frac{\partial \phi}{\partial x}\right) \right.$$

$$- \frac{\partial}{\partial x}\left(\eta(\theta)\eta'(\theta)\frac{\partial \phi}{\partial y}\right)$$

$$\left. + (1-c)Q^A(T,\phi) + cQ^B(T,\phi) \right\}. \quad (21)$$

To conduct the numerical simulations we referred to the phase diagram of an ideal solution of silicon (solvent) and germanium (solute), using the data summarized in Table I and the solute diffusivity in the solid phase was estimated as $D_s = 10^{-6} \times D_l$. However, due to limitations of computational resources, we were forced to use some approximations elucidated below.

In two dimensions the numerical cost of the solution is dramatically dependent on the interface thickness, increasing as h^{-4}. In this study, along the lines suggested by Wheeler, Murray, and Schaefer [26] and Caginalp and Socolovsky [27], the value selected for the interface thickness ($h^{A,B} = 4.2 \times 10^{-6}$ cm) is small compared to the lowest geometric scale that characterizes the process, namely, the radius of curvature of the dendrite tip and, nevertheless, more than 10 times greater than the actual values.

As the diffusivities of the phase and the concentration fields are quite different, Eqs. (13) and (21) should be discretized with different resolution in the time domain, with the finer grid fixing the numerical cost. To overcome this difficulty and to allow a coarser time grid, we decided to reduce the diffusivity of the phase field in Eq. (21), choosing for $\beta^{A,B}$ values about 10 times lower than realistic ones, namely, $\beta^A = 13.48$ cm s^{-1} K^{-1} and $\beta^B = 16.91$ cm s^{-1} K^{-1}. Fixing the surface tension as $\sigma^A = 3.949 \times 10^{-5}$ J/cm^2 and $\sigma^B = 2.806 \times 10^{-5}$ J/cm^2 and with a length scale $\xi = 2.1 \times 10^{-4}$ cm, the model parameters become $W^A = 0.073\,51$, $W^B = 0.072\,62$, and $m^A = m^B = 21.416$.

III. NUMERICAL METHOD

Equations (13), (14), and (21) have been solved in the computational domain $0 \leq x \leq x_m$, $0 \leq y \leq y_m$, with $x_m = 7.16$ and $y_m = 2.40$. For the phase and concentration fields we imposed cyclic boundary conditions at $y = 0$, y_m and flux-

less conditions at $x=0$, x_m. Transparent conditions were chosen for the temperature at $x=0$, x_m. An explicit Euler integration scheme was employed to advance the solution forward in time and second-order central differences were used to discretize the Laplace operator. To ensure an accurate resolution of both the phase and the concentration profiles the grid spacing was selected as $\Delta x=\Delta y=8\times10^{-3}$ and a time step $\Delta t=3.5\times10^{-7}$ was required for numerical stability. The process was followed up to a time $t_{max}=14 \times10^{-3}$, resulting in 40 000 time steps for each simulation. It required more than 24 h on a workstation with a single processor operating at about 30 Mflops. To verify the consistency of the numerical scheme, at each time step the solute conservation was checked and in all the simulations was verified within 0.01%. The initial temperature profile is defined as

$$T(x,0)=\bar{T}_I+G(x-x_0). \tag{22}$$

A phase boundary at temperature $\bar{T}_I$ separates a solid region ($x<x_0$, $\phi=0$, $c=c_{-\infty}$) from the liquid region ($x>x_0$, $\phi=1$, $c=c_{+\infty}$); the initial concentration values in the two phases correspond to equilibrium at $T=\bar{T}_I$. Then the temperature profile is pulled towards the positive x direction starting solidification. As the process enters the oscillatory regime, a periodic corrugation is forced at time t^* on the planar interface located at $x_f(y,t^*)=x^*$; the corrugation, of the form $x_f(y,t^*)=x^*+A\sin(2\pi fy/y_m)$, with $A=0.05$ and $f=16$, is sufficient to activate the two-dimensional dynamics and the banded structure formation.

IV. FRONT DYNAMICS AND BANDED STRUCTURES FORMATION: RESULTS OF THE NUMERICAL SIMULATIONS

A. One-dimensional solution of the model

The loss of interface stability is expected when the isotherm velocity is fixed in the region of positive slope of the $T_I(v)$ curve, corresponding to the unstable planar growth branch. Then, to determine the range of parameters where bands formation could occur, we characterized the one-dimensional dynamics of the process.

The initial concentration of the alloy was set to $c_{-\infty}=0.046\,842$ in the solid phase and $c_{+\infty}=0.117\,54$ in the liquid phase, corresponding to an equilibrium temperature $\bar{T}_I=1660$ K. To force steady growth we fixed the temperature gradient just above the stability limit, determined empirically for each simulation. In these conditions, after an initial transient, solidification proceeded at a constant rate and with uniform concentration $c_{+\infty}$ in the solid phase. The solute segregation on the moving front was evaluated by computing the minimum and maximum values c_s^*, c_l^* of the solute concentration across the interface and defining the partition coefficient as $k(v)=c_s^*/c_l^*$ and the interface temperature was determined by interpolating the temperature field at $x(\phi=0.5,t)$.

Figure 1 shows the partition coefficient versus the growth velocity v. The solids circles refer to the results of the present simulations, while the solid line is drawn according to the predictions of the continuous growth model in the
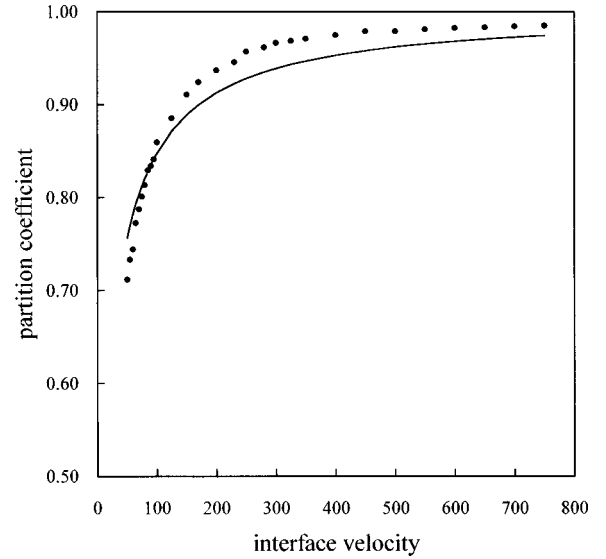

FIG. 1. Partition coefficient $k(v)$ for the one-dimensional solution of the phase-field model (dots) and as predicted by the continuous growth model with $k_e=0.398$ and $v_d=34$ (solid line).

limit of very dilute solutions, which give

$$k(v)=\frac{k_e+v/v_d}{1+v/v_d}. \tag{23}$$

Here k_e is the equilibrium segregation coefficient and v_d is a diffusional velocity given by $v_d=D/a$, D being an interface diffusivity and a the width of the phase transition layer. The best fit was found at $v_d=34$, which is a reasonable value referring to the actual values of the interface solute diffusivity and interface thickness.

In Fig. 2 we show the dependence of the interface temperature on velocity (solid circles) along with the results of the continuous growth model (solid line) expressed by
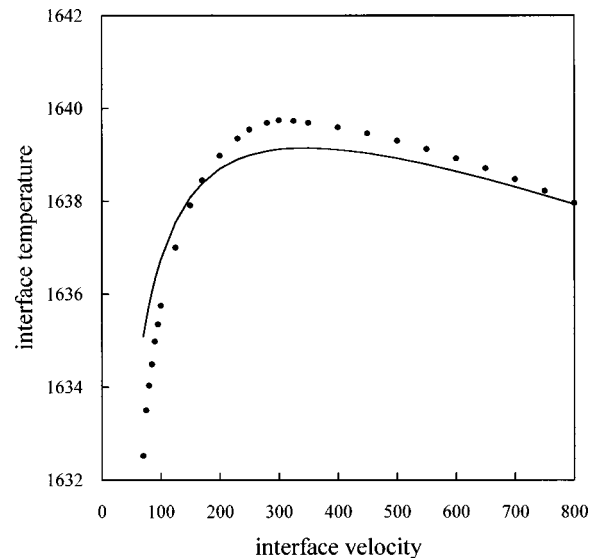

FIG. 2. Interface temperature versus interface velocity for the one-dimensional solution of the phase-field model (dots) and prediction of the continuous growth model (solid line).
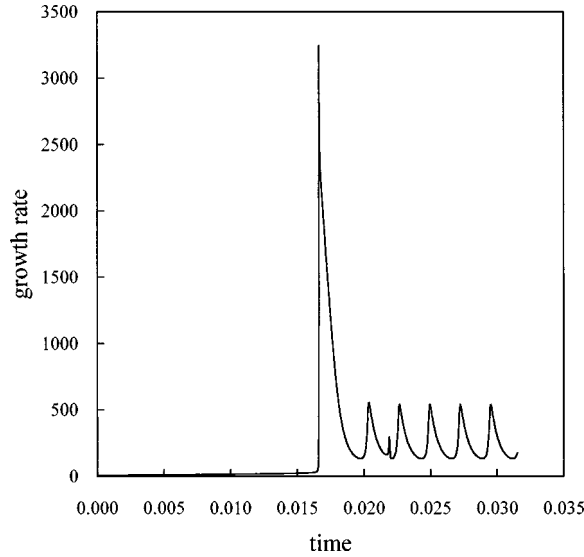
FIG. 3. Periodic variation of the interface velocity versus time for the one-dimensional solution of the phase-field model.
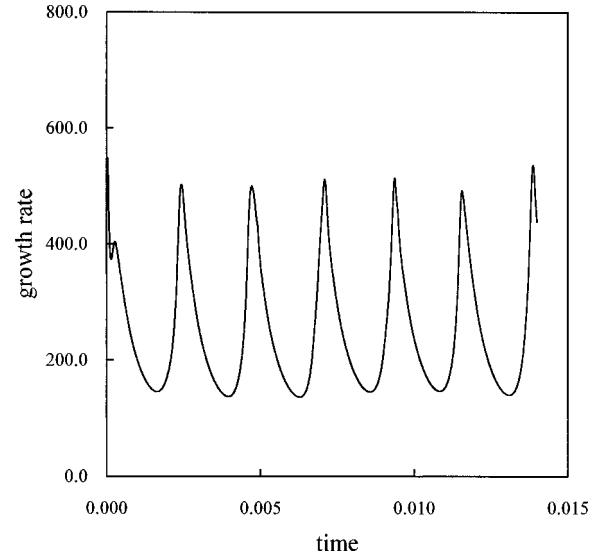

FIG. 4. Periodic variation of the total growth rate versus time for the two-dimensional solution of the phase-field model. The initial perturbation of the planar front fixes the origin of the time axis.

$$T_I(v) = T^A + \frac{m_l c_l}{1-k_e}\{1-k+[k+(1-k)\chi]\ln(k/k_e)\} - \frac{v}{\beta^A},$$
$$(24)$$

where m_l is the slope of the (linearized) equilibrium liquidus line. The parameter χ, ranging from 0 to 1, describes the extent of free-energy dissipation due to solute drag across the interface [28]. With $m_l = -280.7$ the curve is drawn choosing $\chi = 0.65$. We found that the descending branch of the curve better fits the phase-field results with an undercooling coefficient $\beta^A = 10$ slightly lower than the nominal value $\beta^A = 13.48$. Notice that Eq. (24) is obtained starting from a linearized phase diagram and in the limit of low solute concentration, so we do not expect a sharp agreement between the two sets of data.

The positive slope branch of the $T_I(v)$ dependence extends up to $v = 300$, where the maximum is found. Choosing the isotherm velocity V_0 in this region and a temperature gradient below the stability limit should result in an oscillatory dynamics of the solidification front. This prediction is confirmed in Fig. 3, where the interface velocity is represented versus time for $V_0 = 247.5$ and $G = 10$ K; the process never reaches a steady regime and the interface velocity continuously oscillates around the average value V_0.

B. Two-dimensional dynamics: Transition to dendritic growth and banded structure formation

To investigate the growth of the banded structure, following the indications of the previous results, we fix the same operating point, i.e., $c_{+\infty} = 0.117\,54$, $c_{-\infty} = 0.046\,842$, $\bar{T}_I = 1660$ K, $V_0 = 247.5$, and $G = 10$ K. The anisotropy parameter is selected as $\gamma = 0.04$. The perturbation is injected on the planar front after the first peak of the interface velocity at $t^* = 1.82 \times 10^{-2}$, with the front located at $x^* = 2.52$. As it is the beginning of the two-dimensional dynamics in which we are now interested, henceforth the zero of the time axis will be shifted at t^*.

Solidification proceeds characterized by large and periodic variations of the total growth rate, as shown in Fig. 4. It is worth observing (see Fig. 3 for a comparison) that the oscillatory dynamics is essentially the same in one as well as in two dimensions, with the same period of the oscillations; the only significant difference we could detect is the slight fluctuation of the amplitude of the peaks in the two-dimensional solution.

Figure 5 is the space-time portrait of the solidification front, which is identified at $\zeta(y,t) = x(\phi = 0.5, y, t)$. We show 100 snapshots of $\zeta(y,t)$ equally spaced in time; the first and the last curves from the bottom are taken at $t = 1.4 \times 10^{-4}$ and 1.4×10^{-2}, respectively. To focus on the two-dimensional dynamics we represent, along the x direction, only a section of the computational domain, from $x = x^* - 0.16$ (the zero of the vertical scale) to $x = x_m$. The initial perturbation is injected in the high-velocity portion of the cycle and, as shown by the figure, is rapidly reabsorbed. The interface slows down and planar growth proceeds until, near the minimum of the interface velocity, the front breaks into a pattern that still keeps memory of the initial corrugation. The dendrite tips grow faster towards the x direction and grooves are formed. However, now the interface velocity is lower than the isotherm velocity and steady growth is forbidden: The solidification front accelerates and when the absolute stability limit is reached we observe the transition from dendritic to planar growth. The process continuously repeats itself; it is worth observing that after the first cycle the dendritic pattern seems no longer correlated to the initial perturbation.

On the same portion of the computational domain we show in Fig. 6 the contour plot of the concentration field at $t = 1.4 \times 10^{-2}$. In order of decreasing darkness the four zones represent values of the solute concentration $c \leq 0.116$, $0.116 < c \leq 0.118$, $0.118 < c \leq 0.120$, and $c > 0.120$. The banded structure of the solidified alloy here is clearly recognizable. A comparison with Fig. 5 indicates that planar growth corresponds to microsegregation-free regions, with the solute concentration near the nominal concentration of
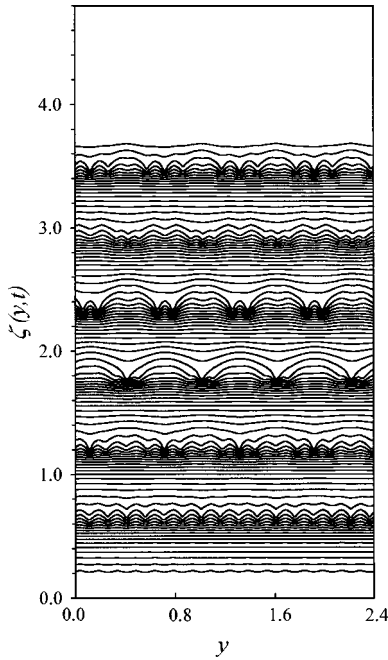
FIG. 5. Dynamical evolution of the solidification pattern. The curves represent 100 different snapshots of the solid-liquid interface taken at equally spaced instants of time; the first and the last curves from the bottom are taken at $t=1.4\times10^{-4}$ and 1.4×10^{-2}, respectively. To focus on the two-dimensional dynamics only a section of the computational domain is represented, from $x=x^*-0.16$ (the zero of the vertical axis) to $x=x_m$.

the alloy. The transition to dendritic growth results in an irregular solute distribution with regions where solute is accumulated, corresponding to the grooves of the solidification pattern.

A more detailed analysis of the front dynamics is allowed by observing Fig. 7, where the radius of curvature and the velocity of the tip located at $y=1.384$ are followed along the third cycle and represented versus the interface position. The fast growth of the dendrite tip corresponds to the decrease of the tip radius at the beginning of the cycle; then the interface is restabilized and the radius of curvature diverges. When the interface velocity reaches its minimum a new tip is formed; inspection of Fig. 5 confirms that the new dendrite is characterized by a much smaller radius of curvature. The periodic breakdown between dendritic and planar growth is the basis of the phenomenological model proposed by Carrard *et al.* [10] to explain the emergence of the banded structure. These authors assume that during the high-velocity section of the cycle the velocity and temperature of the planar front evolve along the stable branch of the steady $T_I(v)$ curve shown in Fig. 2. T_I increases and v decreases: When the maximum of the curve is reached planar growth is no longer possible, as the up-sloping branch corresponds to unstable solutions. Then it is assumed that the front velocity changes instantaneously and the operating point is shifted to a steady dendritic branch, with a much lower velocity. Now T_I decreases and v increases as the dendritic branch is down sloping in the (T_I,v) plane [10]. In this section of the cycle the velocity of the dendrite tips is lower than the isotherm velocity V_0: The interface undercooling increases until with an instanta-
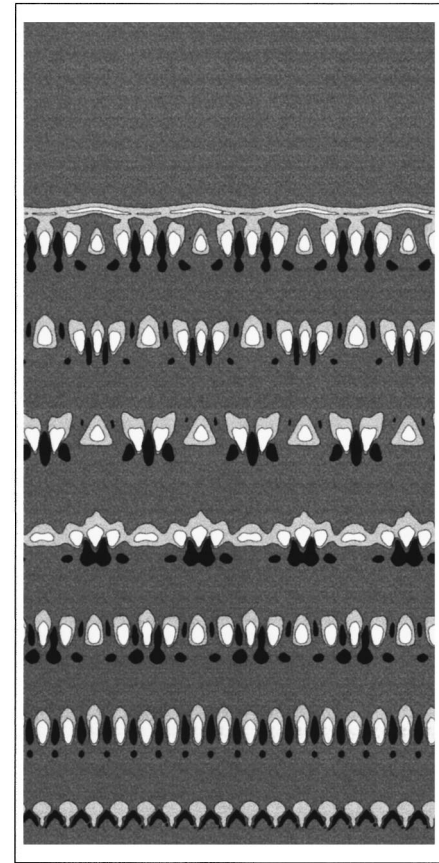

FIG. 6. Contour plot of the concentration field at $t=1.4\times10^{-2}$. In order of decreasing darkness the four zones represent values of the solute concentration $c\leqslant0.116$, $0.116<c\leqslant0.118$, $0.118<c\leqslant0.120$, and $c>0.120$. The portion of the computational domain represented in this figure is the same as in Fig. 5, i.e., $x^*-0.16\leqslant x\leqslant x_m$, $0\leqslant y\leqslant y_m$.
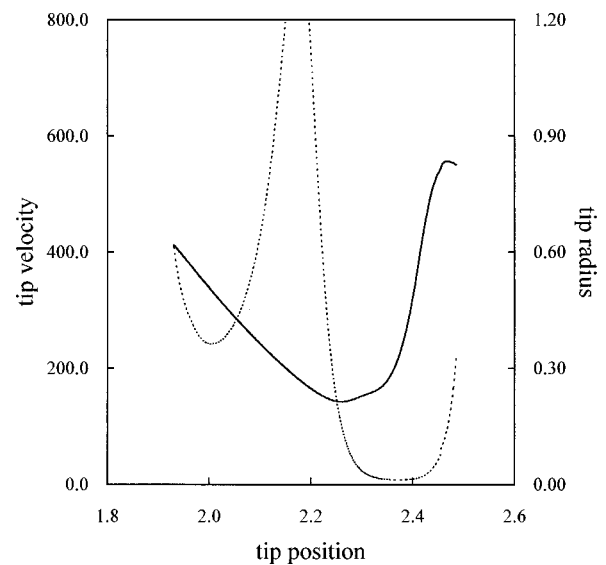

FIG. 7. Tip velocity (solid line) and tip radius (dotted line) versus the x coordinate of the tip position along the third cycle described by the solidification process. The zero of the x axis is chosen at $x=x^*-0.16$, following the same convention as in Fig. 5; the tip of the dendrite is located at $y=1.384$.
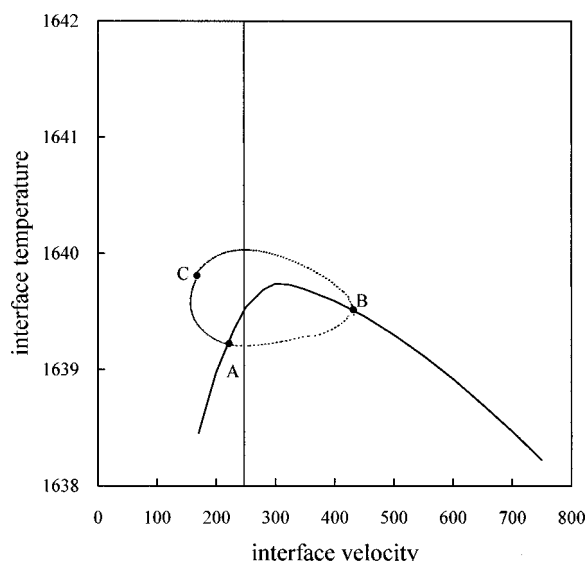
FIG. 8. Orbit followed by the tip temperature and velocity in the (T,v) plane (solid dots), along the first cycle of the process. The dendrite tip is the one located at $y = 1.24$. The solid line refers to the steady solution of the present model. The vertical line represents the pulling velocity V_0. The meaning of the points A,B,C is illustrated in the text.

neous transition the operating point reaches the high-velocity planar branch and the cycle repeats itself.

The main qualitative aspects of the above picture are confirmed by the results of the present simulations. We detected also significant deviations, which will be illustrated in the following. In Fig. 8 we represent in the (T,v) plane the cycle followed by the tip temperature versus the tip velocity. For the reader's commodity we also superimpose the $T_I(v)$ curve for planar growth obtained with the one-dimensional simulations. At low velocities the interface develops the dendritic pattern and cools down. Then the orbit traverses the steady $T_I(v)$ curve at point A, where the front velocity is not far from V_0 and with a strong acceleration reaches point B located on the stable branch; the dendritic pattern is suppressed and the front is restabilized. Here the interface velocity is higher than V_0 and the interface warms up; solidification is decelerated and the process evolves towards point C, where the planar front again breaks into dendrites. The orbit shows a regular shape and we cannot detect instantaneous transitions of the front velocity (which should be represented by horizontal jumps at constant temperature). Moreover, at high velocities, along the down-sloping portion of the cycle, the orbit substantially diverges from the steady $T_I(v)$ curve. These discrepancies trace their roots to the diffuse interface characteristic of the phase-field model. Carrard *et al.* assume an instantaneous relaxation of the solute field

across the interface to the steady configuration; actually, the relaxation time is of the order of $\tau \sim a/v_d$, a being the interface width, and the approximation works only when the transient characteristic time is much larger than τ (or the characteristic frequency is much smaller than $1/\tau$). In the process under consideration τ is of the order of 10^{-3} and the fast transients shown in Fig. 4 exhibit Fourier components comparable to $1/\tau$, then the full time-dependent dynamics described by the present model deviates from the predictions of the quasisteady approximation.

V. CONCLUSIONS

In summary, we used the phase-field model to analyze the emergence, the formation, and the characteristics of the banded structures observed in rapidly solidified alloys. The main results of this study show the following.

(i) The oscillatory instability of the solidification front, due to the nonmonotonic dependence of the $T_I(v)$ curve, actually leads, in a nonlinear regime, to periodic variations of the interface velocity and temperature, reflecting in periodic structures of the solidified alloy.

(ii) A periodic breakdown of the planar front during the low-velocity section of the cycles originates a dendritic pattern that is responsible for the formation of the dark bands. The light bands are the result of a restabilization of the planar front at high velocities. In this respect our results agree with the predictions of the phenomenological model of Carrard *et al.* [10].

(iii) The phase-field model accounts for the full time-dependent interface dynamics. In contrast, the free-boundary approach is based on a quasistationary model of the interface boundary conditions and fails to describe accurately the fast transients characteristic of the band formation.

Due to numerical tractability, in this study we neglected the latent heat released at the solid-liquid interface, assuming an infinite thermal diffusivity. As shown by Karma and Sarkissian [13], relaxing this approximation leads to an increase of the effective temperature gradient probed by the advancing front and to a reduction of the parameters range where the oscillatory instability should be expected; nonetheless, the basic mechanism underlying the formation of the banded structures should have been properly evidenced. In view of future extensions and refinements in this subject, it is worth noting that the phase-field model allows an easy description of rapid solidification processes even for concentrated solutions, with no limitations due to the actual shape of the alloy phase diagram, while at present the free-boundary approach can be applied only to very dilute solutions, when the alloy phase diagram can be conveniently linearized.

[1] M. Zimmermann, M. Carrard, and W. Kurz, Acta Metall. **37**, 3305 (1989).

[2] M. Zimmermann, M. Carrard, M. Gremaud, and W. Kurz, Mater. Sci. Eng., A **134**, 1278 (1991).

[3] M. Gremaud, M. Carrard, and W. Kurz, Acta Metall. Mater. **38**, 2587 (1990).

[4] W. J. Boettinger, D. Shechtman, R. J. Schaefer, and F. S. Biancaniello, Metall. Trans. A **15**, 55 (1984).

[5] W. W. Mullins and R. F. Sekerka, J. Appl. Phys. **35**, 444 (1964).

[6] S. R. Coriell and R. F. Sekerka, J. Cryst. Growth **61**, 499 (1983).

[7] G. J. Merchant and S. H. Davis, Acta Metall. Mater. **38**, 2683 (1990).

[8] M. J. Aziz, J. Appl. Phys. **53**, 1158 (1982).

[9] M. J. Aziz and T. Kaplan, Acta Metall. **36**, 2335 (1988).

[10] M. Carrard, M. Gremaud, M. Zimmermann, and W. Kurz, Acta Metall. Mater. **40**, 983 (1992).

[11] D. A. Huntley and S. H. Davis, Acta Metall. Mater. **41**, 2025 (1993).

[12] A. Karma and A. Sarkissian, Phys. Rev. Lett. **27**, 2616 (1992).

[13] A. Karma and A. Sarkissian, Phys. Rev. E **47**, 513 (1993).

[14] M. Conti, Phys. Rev. E **56**, R6267 (1997).

[15] O. Penrose and P. C. Fife, Physica D **43**, 44 (1990).

[16] A. A. Wheeler, W. J. Boettinger, and G. B. McFadden, Phys. Rev. A **45**, 7424 (1992).

[17] A. A. Wheeler, W. J. Boettinger, and G. B. McFadden, Phys. Rev. E **47**, 1893 (1993).

[18] G. Caginalp and W. Xie, Phys. Rev. E **48**, 1897 (1993).

[19] G. Caginalp and J. Jones, Ann. Phys. (N.Y.) **237**, 66 (1995).

[20] J. A. Warren and W. J. Boettinger, Acta Metall. Mater. **43**, 689 (1995).

[21] M. Conti, Phys. Rev. E **55**, 701 (1997).

[22] M. Conti, Phys. Rev. E **55**, 765 (1997).

[23] M. Conti, Phys. Rev. E **56**, 3717 (1997).

[24] M. Conti (unpublished).

[25] S. L. Wang, R. F. Sekerka, A. A. Wheeler, B. T. Murray, S. R. Coriell, R. J. Braun, and G. B. McFadden, Physica D **69**, 189 (1993).

[26] A. A. Wheeler, B. T. Murray, and R. J. Schaefer, Physica D **66**, 243 (1993).

[27] G. Caginalp and E. A. Socolovsky, J. Comput. Phys. **95**, 85 (1991).

[28] M. J. Aziz and W. J. Boettinger, Acta Metall. Mater. **42**, 527 (1994).